

Highly Crystallized Prussian Blue with Enhanced Kinetics for Highly Efficient Sodium Storage

Mingsheng Qin, Wenhao Ren, Ruixuan Jiang, Qi Li,* Xuhui Yao, Shiqi Wang, Ya You,* and Liqiang Mai*



Cite This: *ACS Appl. Mater. Interfaces* 2021, 13, 3999–4007



Read Online

ACCESS |



Metrics & More



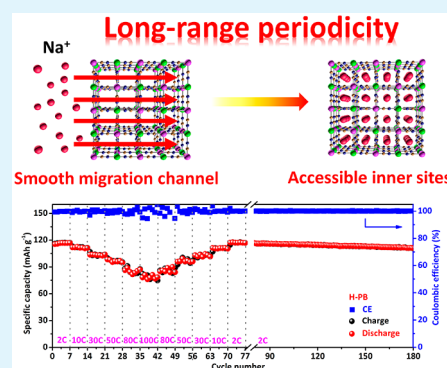
Article Recommendations



Supporting Information

ABSTRACT: Prussian blue analogs (PBAs) featuring large interstitial voids and rigid structures are broadly recognized as promising cathode materials for sodium-ion batteries. Nevertheless, the conventionally prepared PBAs inevitably suffer from inferior crystallinity and lattice defects, leading to low specific capacity, poor rate capability, and unsatisfied long-term stability. As the Na^+ migration within PBAs is directly dependent on the periodic lattice arrangement, it is of essential significance to improve the crystallinity of PBAs and hence ensure long-range lattice periodicity. Herein, a chemical inhibition strategy is developed to prepare a highly crystallized Prussian blue ($\text{Na}_2\text{Fe}_4[\text{Fe}(\text{CN})_6]_3$), which displays an outstanding rate performance (78 mAh g^{-1} at 100 C) and long life-span properties (62% capacity retention after 2000 cycles) in sodium storage. Experimental results and kinetic analyses demonstrate the efficient electron transfer and smooth ion diffusion within the bulk phase of highly crystallized Prussian blue. Moreover, *in situ* X-ray diffraction and *in situ* Raman spectroscopy results demonstrate the robust crystalline framework and reversible phase transformation between cubic and rhombohedral within the charge–discharge process. This research provides an innovative way to optimize PBAs for advanced rechargeable batteries from the perspective of crystallinity.

KEYWORDS: Prussian blue analogs, high crystallinity, solid-state diffusion, sodium ion batteries, crystal structure



1. INTRODUCTION

The increasing exhaustion of fossil energy and the resulting environmental problems made it urgent to resort to sustainable energy sources. Energy storage systems are critical for integrating intermittent renewable energies into large-scale grids.^{1,2} Lithium-ion batteries (LIBs), which were applied in 1991 and have achieved great success in portable electronics since then, are widely recognized as unaffordable for industrial-scale energy storage because of the low resource reserves, uneven distribution, and rising cost.^{3,4} At the same time, sodium-ion batteries (SIBs) have grabbed much attention by virtue of the abundant reserves and wide availability.⁵ Also, the similar chemical properties of sodium and lithium elements make SIBs more advantageous over LIBs in some future energy storage applications.^{6,7}

Although numerous advanced cathode materials have been demonstrated to be feasible for SIBs, developing satisfactory electrode materials with high energy density, great power capability, and low cost is still the bottleneck for the scale-up applications of SIBs in the following years.^{8,9} Among various cathode materials including Prussian blue analogues (PBAs), polyanion compounds, organic materials, and layered oxides, PBAs are promising cathode materials because of the advantages of open interstitial channels, low cost, and facile synthesis.^{10–12} Previous reports have demonstrated that the Na^+ storage

performance of PBAs is not only closely correlated to the confined interstitial sites but also associated with the smooth ion diffusion channels.^{13,14} However, the available interstitial spaces formed by cyanic bridging and transition metals are generally restricted by the lattice defects and interstitial water, which results in inferior Coulombic efficiency and fast capacity deterioration in SIBs.^{15,16} To overcome this problem, most research focuses on preparing a robust Prussian blue structure with suppressed vacancies and interstitial water.^{17,18} You et al. exemplified high-quality Prussian blue (PB) crystals with less vacancies, which feature high capacity and long life-span properties.¹⁹ Song et al. studied the correlations between interstitial water and electrochemical properties in hexacyano-metallates, demonstrating that elimination of interstitial water results in phase transformation and an improved charge storage performance.²⁰ Unfortunately, the continuous Na^+ migration paths, which are enabled by the periodic lattice arrangement and hence play significant roles in solid-state diffusion, have long

Received: November 10, 2020

Accepted: January 4, 2021

Published: January 13, 2021



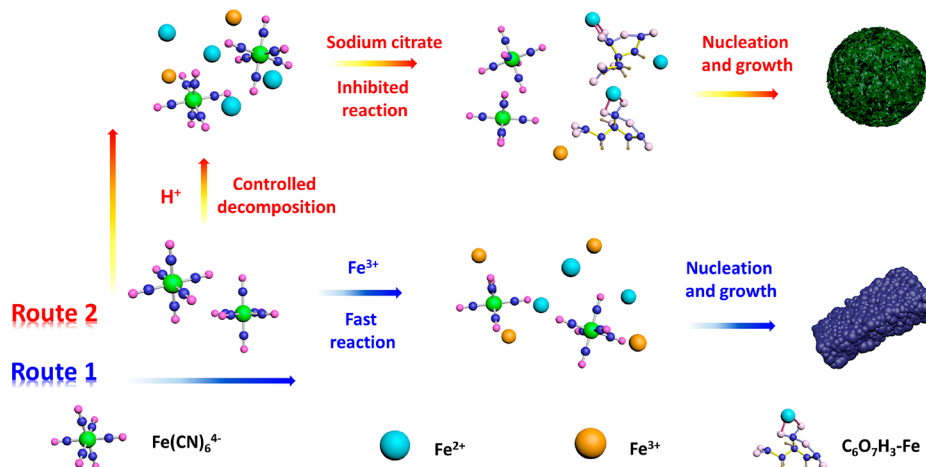


Figure 1. Schematic diagram for the synthesis of Prussian blue (Route 1, the conventional coprecipitation method for L-PB; Route 2, the advanced chemical-inhibited process for H-PB).

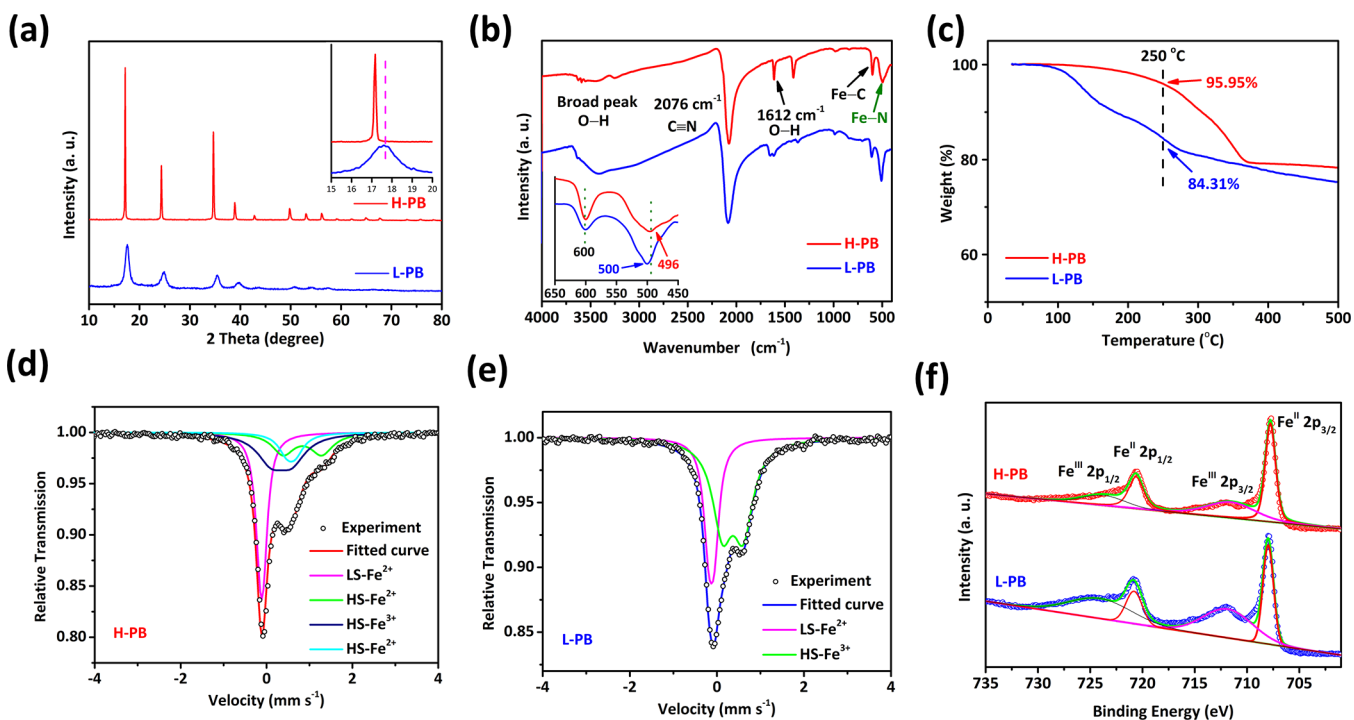


Figure 2. Characterizations of the as-synthesized H-PB and L-PB. (a) XRD patterns. (b) FT-IR spectra. (c) TG curves. Mossbauer spectrum of (d) H-PB and (e) L-PB. (f) Fe 2p XPS spectra.

been ignored. Moreover, the crystallinity, a critical parameter in the crystal structure, is also urgently worthy of discussion to clarify the dynamic controlling effects on the bulk properties of PBA materials.

Here, we develop a highly crystallized Prussian blue (H-PB) cathode material with efficient kinetics and robust structure through a chemical inhibition strategy. The structural and molecular deviations between H-PB and low-crystallized Prussian blue (L-PB) were systematically investigated. Interestingly, H-PB exhibited a much improved solid-state diffusion efficiency because of the smooth migration channels, resulting in unprecedented sodium storage performance. The fast electronic and ionic transfer were systematically studied by dynamic analyses and experiments. Furthermore, the inherent storage mechanism and corresponding structure–performance relationships were revealed by the *in situ* X-ray diffraction (XRD) and *in*

situ Raman techniques. More importantly, the full cell assembled with H-PB and hard carbon as cathode and anode materials presented a good electrochemical performance, manifesting the feasibility of H-PB electrode material for practical application.

2. RESULTS AND DISCUSSION

2.1. Morphology and Structure. L-PB was synthesized by a conventional coprecipitation method as depicted by route 1 in Figure 1.²¹ The dark blue sediment precipitated immediately once blending Fe^{3+} and $[\text{Fe}(\text{CN})_6]^{4-}$ in an aqueous solution (Figure S1). The fast and uncontrollable coordination process inevitably leads to agglomerated nanoparticles with substantial defects and coordinated water. To deliberately regulate the nucleation and crystal growth rate, a chemical-inhibited strategy was proposed under the complementary assistance of H^+ and

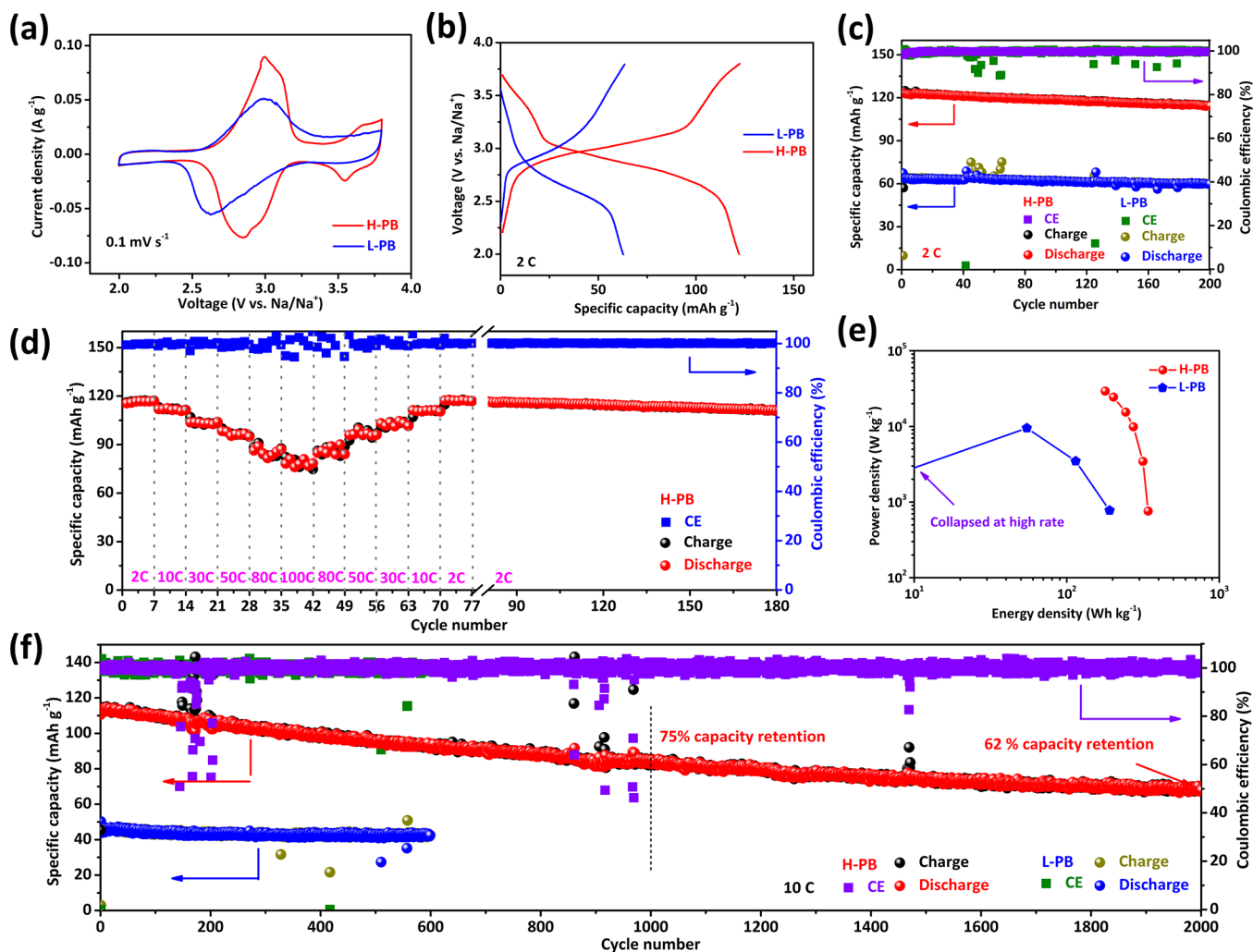


Figure 3. Electrochemical performance of H-PB and L-PB cathode materials. (a) The third-cycle CV profiles. (b) The typical galvanostatic charge/discharge curves. (c) Cycling performance at 2 C. (d) Rate performance at various current densities from 2 to 100 C. (e) Ragone plots of the electrode. (f) Long-term cycling performance at 10 C for H-PB and L-PB.

citrate. As shown by route 2, $[\text{Fe}(\text{CN})_6]^{4-}$ decomposes slowly under the acid circumstance and generates numerous Fe^{2+} ions.^{19,22} Afterward, citrate bonds with these newly formed Fe^{2+} and hence effectively suppresses the oxidation of Fe^{2+} . Because of the lower binding energy of Fe^{2+} - $[\text{Fe}(\text{CN})_6]^{4-}$ complex relative to Fe^{2+} -citrate, Fe^{2+} tends to gradually dissociate from citrate and eventually coordinates with ferrous cyanide as the reaction goes on, forming H-PB crystals.²³ The introduction of sodium citrate largely avoids the direct and rapid reaction between Fe^{2+} and ferrous cyanide, so as to decrease the coordination reaction rate and further ensure plenty of time for nucleation and crystal growth (Figure S1). By this way, the crystallinity of Prussian blue was subtly tailored via adjusting the concentration of sodium citrate (Figure S2). As displayed in Figure S3, H-PB shows a microsphere morphology with sizes ranging from 3 to 6 μm . Transmission electron microscopy (TEM) images show that numerous nanoparticles accumulated and self-assembled to form a secondary particle (Figure S4). In addition, the low surface area could alleviate side reactions at the cathode–electrolyte interface.^{18,24} As a comparison, L-PB is composed of agglomerated nanoparticles and shows irregular size and shape (Figure S5). Element mapping presented in Figure S3 shows a uniform dispersion of Na, C, N, Fe, and O in

H-PB, which is also confirmed by XPS results (Figures S6 and S7). Inductively coupled plasma analysis (ICP) results reveal that the stoichiometric compositions of H-PB and L-PB are $\text{Na}_2\text{Fe}_4[\text{Fe}(\text{CN})_6]_3$ and $\text{Na}_{0.6}\text{Fe}_4[\text{Fe}(\text{CN})_6]_3$, respectively, demonstrating the Na-rich characteristic of H-PB (Table S1). In this manuscript, we prefer to use the simplified formulas $\text{Na}_2\text{Fe}_4[\text{Fe}(\text{CN})_6]_3$ and $\text{Na}_{0.6}\text{Fe}_4[\text{Fe}(\text{CN})_6]_3$ without showing defects for concisely denoting the as-prepared samples, in agreement with the commonly used methods in literature.^{24,25}

The crystal structure and purity of the prepared H-PB and L-PB were identified by the powder XRD techniques. As exhibited in Figure 2a, the diffraction peaks of H-PB, in contrast with L-PB, show stronger intensity and narrower full width at half-maximum (fwhm), supporting a higher crystallinity of H-PB. The detailed structure information can be obtained from Rietveld-refined XRD results (Figure S8). The structural comparison of two samples is listed in Table S2. Both H-PB and L-PB possess face-centered cubic lattice (fcc) with a space group of $F43m$.²⁶ Obviously, the calculated lattice constants of H-PB (10.36 Å) is bigger than that of L-PB (10.04 Å). This is attributed to the enriched contents of Na^+ within the pristine lattice of H-PB, which expands the lattice framework.²⁷ The typical local structure is presented in Figure S8. FeC_6 and FeN_6

octahedrons are alternately bridged by the linear groups of $C\equiv N$, forming a rigid double perovskite framework. As a result, the open lattice provides three-dimensional channels for efficient Na^+ diffusion.^{28,29} The subtle discrepancies in molecular structures of two samples were revealed by Fourier transform infrared spectra (Figure 2b). Notably, an intense adsorption peak centering around 2076 cm^{-1} is attributed to the stretching pattern of cyanide groups.^{30,31} In addition, two distinct peaks located at 600 and 496 cm^{-1} belong to $Fe-C$ and $Fe-N$ stretching patterns in H-PB samples. The shift of $Fe-N$ to higher wavenumber (500 cm^{-1}) in L-PB manifests the higher average valence of the Fe coordinated with N.^{32,33} Moreover, the $H-O-H$ bending and broad $O-H$ stretching modes, arising from lattice water and adsorbed water, are revealed by the peaks centered at 1612 and 3560 cm^{-1} , respectively.^{34,35} Water molecule tends to accumulate at lattice vacancies and coordinate with Fe octahedron to maintain the electroneutrality. As verified by the thermogravimetric analysis (TGA) in Figure 2c, the weight losses below $250\text{ }^\circ\text{C}$ were noticed in two samples with that below $200\text{ }^\circ\text{C}$ attributing to the elimination of adsorbed H_2O and that ranging from 200 to $250\text{ }^\circ\text{C}$ to the removal of the lattice water due to the strong attraction between water molecules and Fe^{3+} . The only 4% weight loss in H-PB demonstrates a notable suppression on the water content by the chemical-inhibited strategy. Further temperature rise above $250\text{ }^\circ\text{C}$ results in the decomposition of the framework.^{20,34} The nitrogen adsorption-desorption isotherms displayed in Figure S9 shows that H-PB has a low surface area of $3.5\text{ m}^2\text{ g}^{-1}$ because of its dense microsphere structure. The agglomerated nanoparticles of L-PB, by contrast, shows a higher surface area around $221.3\text{ m}^2\text{ g}^{-1}$. Interestingly, H-PB exhibits better electrochemical performance even without large surface area, suggesting the intrinsic crystal quality in PB is of prime significance for SIBs.

Raman spectra were collected on two samples to determine the valence states of iron (Figure S10). Peaks situated at 2110 and 2150 cm^{-1} represent the vibration of the cyanide group coordinated with Fe^{2+} and Fe^{3+} , respectively.³⁶ Compared with L-PB, H-PB shows a much stronger intensity on 2110 cm^{-1} peak, indicating a lower average valence state of Fe. Mössbauer spectra at 298 K were collected to clarify the electronic structure of two samples and the consequences are presented in Figure 2d,e. The detailed fitting parameters are summarized in Table S3, where Q_s denotes the quadrupole splitting and δ represents the isomer shift. Notably, both H-PB and L-PB show typical singlets with negligible values of Q_s for the octahedral low-spin Fe^{2+} (LS Fe^{2+}) in $[Fe^{II}(CN)_6]^{4-}$. It is worth noting that three doublets with isomer shifts of 0.370 , 0.600 , and 0.863 can be observed in H-PB. All of them are assigned to the HS- Fe^{3+} and HS- Fe^{2+} , which are coincide with the Na-rich structure.³⁷ The smaller value of Q_s for $[Fe^{II}(CN)_6]^{4-}$ than that of Fe^{2+} demonstrates more symmetrical coordination environment.²⁷ In contrast, only one doublet of HS- Fe^{3+} with an isomer shift of 0.374 was observed in L-PB, suggesting the high valence state of HS-Fe. X-ray photoelectron spectroscopy (XPS) further verified the Fe states in H-PB and L-PB. The results are exhibited in Figure 2f, where two distinct peaks situated at 720.7 and 707.0 eV are, respectively, attributed to $Fe^{II}2p_{1/2}$ and $Fe^{II}2p_{3/2}$ within the $[Fe^{II}(CN)_6]^{4-}$ units. The higher binding energy peaks around 724.6 and 711.9 eV are, respectively, associated with $Fe^{III}2p_{1/2}$ and $Fe^{III}2p_{3/2}$.³⁸ Obviously, the relatively weaker peak of Fe^{3+} in H-PB indicates the lower contents of Fe^{3+} in the sample. On the basis of the above analyses, the H-PB exhibits

lower average valence for Fe, which can be attributed to the insertion of more Na^+ ions.

2.2. Charge Storage Performance. The sodium storage capabilities of two samples were evaluated in the half-cell configurations at ambient temperature within a potential range of $2.0-3.8\text{ V}$ (V v. Na/Na^+). Figure 3a shows the third cyclic voltammetry (CV) curves of two samples at 0.1 mV s^{-1} . Obviously, a redox peak situated around 3.0 V can be observed for both samples, while the much higher peak current and larger curve area of H-PB suggest the superior Na^+ diffusion kinetics and higher specific capacity. Also, the H-PB exhibits smaller peak separation compared with L-PB, manifesting lower polarization. An additional pair of peaks that appeared at $3.53/3.51\text{ V}$ for H-PB indicates part of ClO_4^- anions intercalate into the bulk phase of H-PB from the electrolyte, as reported in previous works.^{21,25} However, the insertion of ClO_4^- anions was not observed in L-PB possibly due to the contracted lattice parameter (10.36 \AA for H-PB and 10.04 \AA for L-PB) and blocked migration channels. Moreover, the superior repetition of CV curves in the initial three cycles manifests the high reversibility of H-PB (Figure S11). The typical charge-discharge profiles of two samples at 2 C (1 C is defined as 120 mA g^{-1}) are presented in Figure 3b. H-PB exhibits a long discharge plateau around 2.9 V and a short discharge plateau at 3.5 V , whereas only one plateau at 2.9 V is observed in L-PB. This phenomenon evidently agrees well with the CV profiles. The cycling properties of H-PB and L-PB at 2 C are presented in Figure 3c. The initial charge capacity of H-PB and L-PB are, respectively, 60 mAh g^{-1} and 12 mAh g^{-1} , corresponding to the extraction of 2 and 0.4 Na^+ from the pristine structure (Figure S12). H-PB with high Na^+ contents is more feasible for practical applications because Na^+ only extracts from the cathode side in full batteries. A high discharge capacity around 110 mAh g^{-1} is well maintained after 200 cycles for H-PB with a Coulombic efficiency of virtually 100% . As shown in Figure S13, a smaller voltage hysteresis with complete curve overlapping is observed in H-PB, manifesting faster reaction dynamics. For comparison, only limited capacity of 60 mAh g^{-1} was provided after 200 cycles in L-PB. The hindered capacity can be attributed to the limited accessible sodium storage sites, which is resulted from the lattice defects and coordinated water.^{13,15,39} Galvanostatic cycling was also performed at a high mass loading of 7.2 mg cm^{-2} for H-PB, exhibiting a discharge capacity of 100 mAh g^{-1} after 80 cycles at 2 C (Figure S14). Even confronted with extreme environment, the H-PB was capable of delivering discharge capacities of 93 and 105 mAh g^{-1} , respectively, at 0 to $50\text{ }^\circ\text{C}$ after 100 cycles, as exhibited in Figure S15. The negligible performance degradation after changing temperature demonstrates the adaptability of H-PB to extreme environment.

The rate performances of two samples were further studied with current densities altering from 2 to 100 C . As depicted in Figure 3d, The H-PB delivers reversible capacities of 118 , 110 , 104 , 95 , and 83 mAh g^{-1} along with the current densities ranging from 2 to 80 C . A reversible discharge capacity as high as 78 mAh g^{-1} is still maintained though at a super high rate of 100 C (the current density equals to 12 A g^{-1} and only 3 s for the full discharge process) with about 65.5% capacity retention. Furthermore, the capacity restores to 113 mAh g^{-1} as long as the current density goes back to 2 C . The following stable cycling further demonstrates the superiority of H-PB even after the long-range current fluctuations, yielding the best rate performance of PBAs in nonaqueous SIBs to the best of our knowledge (Table S4). Nevertheless, L-PB exhibits unsatisfied

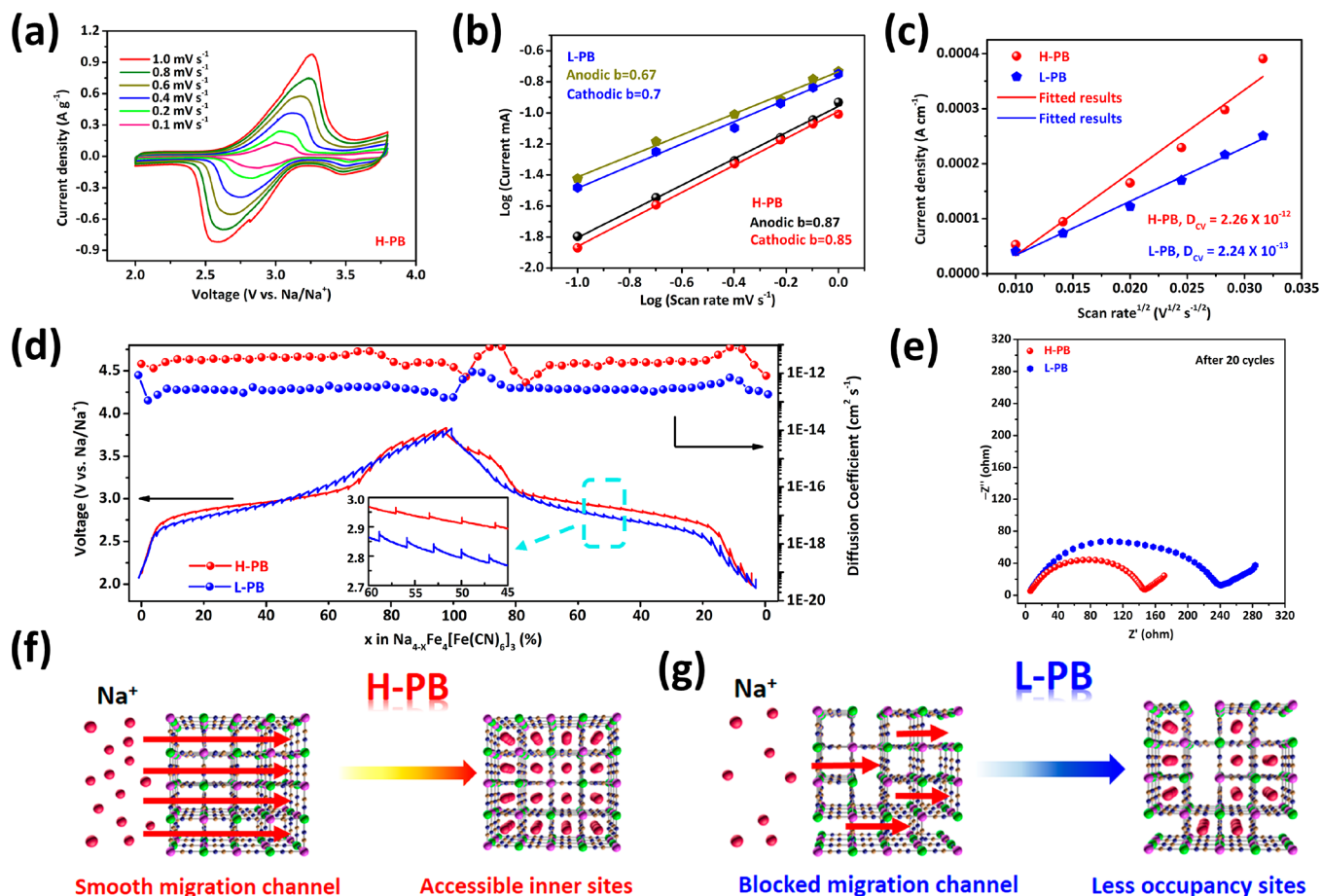


Figure 4. Electrochemical kinetics analyses of sodium storage. (a) Normalized CV curves at various scan rates. (b) Determination of b value from the linear fitting. (c) Calculated apparent diffusion coefficient from multiple CV results. (d) GITT curves and corresponding calculations. (e) Nyquist plots of the cycled H-PB and L-PB electrodes in half-cells. Schematic illustrations for the ion migration in (f) H-PB and (g) L-PB materials.

capacity of 73 mAh g^{-1} at 2 C and eventually cannot supply storage at elevated rates (Figure S16). Moreover, the H-PB exhibits smaller voltage hysteresis and higher capacity retention at each rate (Figure S17). The high crystallinity of H-PB effectively guarantees a robust structure, which can be well preserved even at an ultrahigh current density. Figure 3e shows the Ragone plot of H-PB and L-PB samples. Benefiting from ultrafast reaction kinetics and robust crystal structure, the electrochemical system based on H-PB exhibits substantial power density up to 29.3 kW kg^{-1} and the impressive specific energy density as high as 179 Wh kg^{-1} . Figure 3f shows the long-term stability of two cathode materials at 10 C . Obviously, the H-PB retains a reversible discharge capacity of 70 mAh g^{-1} even after 2000 cycles, about 62% preservation of the initial capacity, corresponding to a fading rate of 0.019% per cycle. By contrast, only 40 mAh g^{-1} is maintained by L-PB, which is too low to satisfy the practical applications.

2.3. Dynamic Analyses. In order to obtain the fundamental understanding of the superior charge-storage performance of H-PB, systematical dynamical analyses including multistep CV, galvanostatic intermittent titration techniques (GITT), and electrochemical impedance spectroscopy (EIS) were employed. Figure 4a depicts the voltammetric sweep data of H-PB varying between 0.1 and 1 mV s^{-1} . Notably, the peak current of H-PB increases with the augment of sweep rates (Figure 4a). The smaller peak separation compared to L-PB suggests the lower polarization in H-PB (Figure S18). The redox kinetics can be

determined via the power-law principle of peak current (I) and sweep rate (V)⁴⁰

$$I = aV^b \quad (1)$$

where both a and b are variable parameters, and b value can be calculated by the tangent of $\log(V)$ and $\log(I)$. Theoretically, faradaic diffusion-limited or capacitive-controlled mechanism can be distinguished by the b value of 0.5 and 1 , respectively. As depicted in Figure 4b, the calculated b values for both L-PB and H-PB are between 0.5 and 1 , indicating that the sodium-storage for two samples is controlled by both intercalation mechanism and capacitive procedure.^{38,40,41} The capacity contributions from different mechanisms are indicated separately in Figure S19. The highly crystallized H-PB features with the periodic lattice arrangement, leading to less Na^+ ions diffusion constraints and higher availability of active sites, and hence contributing to more capacitive-contribution compared to L-PB. Figure 4c exhibits the apparent Na^+ diffusion coefficient (D_{CV}) estimated from multi-step CV results, suggesting the Faradaic diffusion coefficient of 2.26×10^{-12} and 2.26×10^{-13} for H-PB and L-PB, respectively. Furthermore, the apparent diffusion coefficient variations (D_{GITT}) during the entire electrochemical process was calculated from GITT results (Figure S20). As shown in Figure 4d, no sharp decrease in D_{GITT} can be observed within Na^+ insertion/deinsertion, indicating the phase transformation between cubic and rhombohedral phases (as proven in the following discussion) is highly efficient and reversible, and there

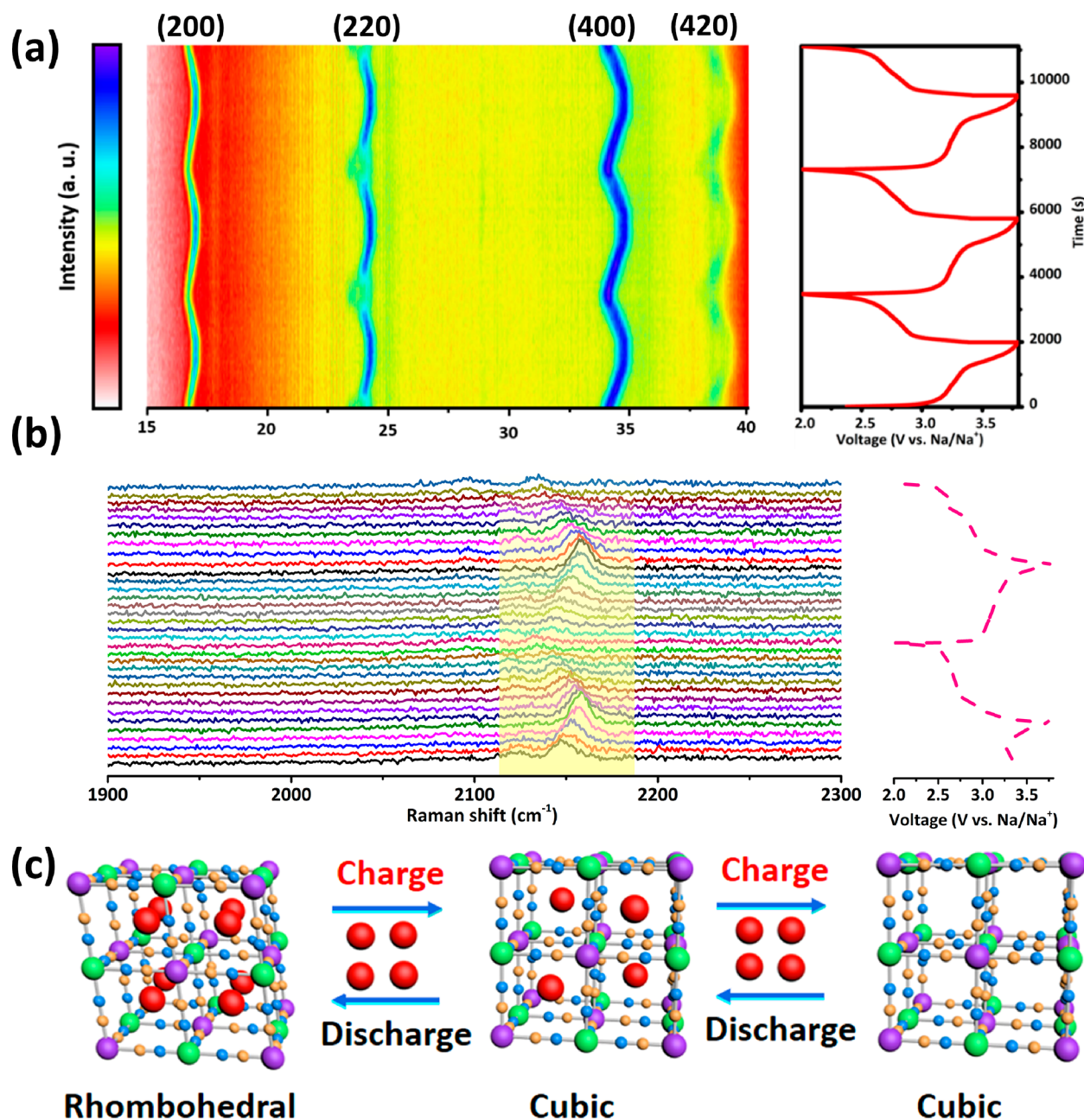


Figure 5. Storage mechanism for H-PB. (a) *In situ* XRD results and corresponding charge–discharge curves. (b) *In situ* Raman spectroscopy. (c) Illustration for the phase transformation during electrochemical process.

are smooth and continual diffusion paths for Na^+ in H-PB. Notably, the calculated D_{GITT} for H-PB ranges from 10^{-11} to 10^{-12} , which is about a magnitude higher than that in L-PB (ranges from 10^{-12} to 10^{-13}), demonstrating faster solid-state diffusion in the bulk phase of H-PB (Figure S21).

The electrochemical kinetics were further revealed via the EIS results. The Nyquist plots of two samples in both pristine and extended cycling are presented (Figure S22 and Figure 4e) with a suppressed semicircle and an oblique line observed in Figure 4e. In general, the diameter of hemicircle within the high-medium frequency zone demonstrates the charge-transfer resistance (R_{ct}), and the oblique line corresponds to the Warburg diffusion in the electrode.³² Notably, the R_{ct} of L-PB (212.6Ω) is larger than that of H-PB (142.1Ω), manifesting the higher charge-transfer resistance (Figure S23). The vacancies in

L-PB break the integrity of the crystal lattice, and therefore hinder the electron transportation along $\text{C}\equiv\text{N}$ skeletons.¹⁹ The semi-infinite diffusion in the bulk phase of Prussian blue can be understood by the oblique line within the low-frequency region. The obtained Warburg coefficients from the fitting line are 5.86 and 2.92 for L-PB and H-PB, which also indicates that the apparent diffusion coefficient (D_{EIS}) of H-PB is improved about an order of magnitude compared with that of L-PB (Figure S22b).

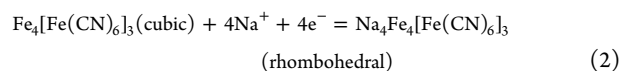
The solid-state diffusion, a key process during the overall electrode reaction, always becomes the limiting factor for the electrochemical performance.^{16,42} In this case, the structural and crystallographic deviations in two samples regulate their electrochemical and kinetic responses. As for H-PB, high crystallization ensures the long-range lattice periodicity, which

promotes Na⁺ diffuse smoothly and continuously along [100] axis via a step-by-step cooperative manner in the framework, resulting in efficient solid-state diffusion.⁴³ Moreover, the integrated crystal structure of H-PB contains less defects and coordinated water, guaranteeing substantial active sites for the Na⁺ insertions. (Figure 4f). Owing to the ultrafast Na⁺ diffusion and efficient electron transfer, the inner active sites can be easily obtained by the inserted Na⁺, and even behave like the surface or the near surface active sites (Figure S24). However, L-PB has a poor lattice periodic arrangement and contracted lattice parameters, which leads to the sluggish ion transfer and inferior charge storage performance. (Figure 4g) Furthermore, the vacancies and coordinated water inhibit the full use of active sites and therefore restrain the efficient sodium storage.^{15,37,39}

2.4. Structural Variations. To track the structural variations of H-PB during the electrochemical process, *in situ* XRD patterns were recorded within 2.0 to 3.8 V (Figure 5a). During the discharge process, the diffraction planes of (200), (220), (400), and (420) shift to lower angles, which means the increase of lattice parameters due to the insertion of Na⁺, and the continuous shift of these peaks strongly suggests a relatively low energy barrier for Na⁺ diffusion in the long periodic framework.^{24,25} A slight broadening of the (400) peak at the end of discharging process is attributed to the internal strain and possible cell orientation of the H-PB (Figure S25). The lattice symmetry is gradually decreased in pristine cubic framework with the accumulation of Na⁺ in lattice, leading to a phase transformation from cubic to rhombohedral as indicated by the peak splits of (220) and (420) planes when discharged to 2.6 V (about 3.2 Na⁺ inserted into the lattice).^{27,38} This structural variation is beneficial to release the internal stress and effectively preserve the integrity of the crystal structure during Na⁺ insertion. During the following charging process, split peaks merge together with the structure changing back from the rhombohedral to the cubic phase. Moreover, all peaks gradually shift to higher angles along with well-preserved peak symmetry and intensity during the charging process, demonstrating the feasible and reversible extraction of Na⁺ from crystal lattice. In the following cycles, the major diffraction peaks are well maintained and the structure variation is highly reversible, giving reasons for the enhanced rate performance and ultralong cycle stability. The crystalline arrangement of H-PB can still be well maintained even after 300 cycles as shown in Figure S26. The morphological evolutions are further compared for H-PB and L-PB (Figure S27), showing well-maintained morphology after cycling for H-PB. For comparison, the *ex situ* XRD was also carried out on L-PB, and a similar peak shift trend is exhibited in Figure S25b. Apparently, the major peaks shift to higher angles upon the charging process and recover in the discharging process, suggesting the shrinking and expansion of lattice. However, L-PB keeps the cubic structure with no phase transformation in the whole electrochemical process. This can be attributed to the relatively shallow intercalation/deintercalation degree of Na⁺ (about 2 Na⁺ involved), which does not induce extensive inner stress and volume variation.^{22,44}

In situ Raman technique was carried out to investigate the active sites upon Na⁺ intercalation/deintercalation because of the sensitivity of C≡N vibration modes to surrounding Fe atoms.^{33,44} As presented in Figure 5b, two characteristic peaks situated at around 2110 and 2150 cm⁻¹, which are assigned to the cyanide (C≡N) group coordinated Fe²⁺ and Fe³⁺, respectively, can be noticed at the initial stage. During charging, the peak centering at 2110 cm⁻¹ gradually decreases to zero,

while the peak situated at 2150 cm⁻¹ shifts to higher wavenumbers and the intensity increases, which clearly show the oxidation from Fe²⁺ to Fe³⁺. On the reverse process, the peak with the high wavenumber recovers to its original stage and even vanishes when discharged to 2 V, manifesting that Na⁺ diffuses into the bulk phase and hence causes the full reduction of Fe³⁺ to Fe²⁺. A similar phenomenon is also observed during the following cycles, suggesting a highly reversible faradic reaction. The above transformation of Fe is also confirmed by *ex situ* FT-IR results (Figure S28). As the cyanide group is closely affected by N coordinated Fe but is unresponsive to C coordinated atoms in FTIR, it is reasonable to distinguish the active couples from two types of Fe atoms.^{45,46} A blue-shift of the cyanide group can be found in FTIR results during the charging process, suggesting the oxidation of N-coordinated Fe²⁺. Also, the peak reversibly recovers to the initial position after discharging, demonstrating the following reduction of N-coordinated Fe³⁺.⁴⁵ On the basis of the above analysis, the charge storage mechanism can be deduced as shown in Figure 5C. A multiple electron involved reaction can be expressed as follows



This Faradic intercalation/deintercalation process is favored for H-PB owing to the fast kinetics and robust structure. Moreover, a theoretical specific capacity of around 120 mAh g⁻¹ can be delivered for the electrode, which satisfies the conditions for scale-up energy storages.

2.5. Na-ion Full Batteries. To demonstrate the feasibility for real-world applications, Na-ion full batteries were evaluated with H-PB cathode and hard carbon anode. Hard carbon was derived from the shaddock peels, featuring low cost and easy availability.⁴⁷ Before the full cell assembly, the detailed characterization and electrochemical performance of hard carbon were measured as exhibited in Figure S29. The assembled full battery was cycled between 1.8 and 3.8 V, exhibiting an initial discharge capacity as high as 126 mAh g⁻¹. After 20 cycles, a reversible capacity of 64 mAh g⁻¹ is maintained (Figure S30). The mediocre storage capability might be attributed to the mismatch between electrodes and electrolyte, but as a prototype the cheap electrode materials and easy production provide a new approach to develop a low-cost storage system for the possible scale-up applications.

3. CONCLUSION

In summary, Prussian blue with high crystallinity was prepared through a chemical inhibition strategy. The long-range periodicity in H-PB ensures efficient electron transfer and continuous ion migration, resulting in enhanced electrochemical dynamics. On the basis of this mechanism, H-PB exhibits an unprecedented rate capability (78 mAh g⁻¹ at 100 C) and superior long-term lifespan (62% preservation after 2000 cycles at 10 C). *In situ* XRD and *in situ* Raman spectroscopy techniques proved the efficient structural transformation (conversion between cubic and rhombohedral phases) and full reaction of active sites (4 Na⁺ involved reaction). Moreover, a full cell assembled by H-PB and hard carbon exhibits good performance. This work provides a new crystal-level strategy to optimize Prussian blue for energy storage.

■ ASSOCIATED CONTENT

■ Supporting Information

The Supporting Information is available free of charge at <https://pubs.acs.org/doi/10.1021/acsami.0c20067>.

Details for structural and electrochemical characterizations, SEM and TEM images of H-PB and L-PB; Rietveld refinements and corresponding local structures for H-PB and L-PB; BET results and Raman spectra for H-PB and L-PB; the CV curves at 0.1 mV s⁻¹ and charge-discharge curves for both H-PB and L-PB; the rate performance of L-PB; the cycling stability of H-PB at varied temperature; schematic of outside-in diffusion pathways; *in situ* XRD results and *ex situ* FT-IR for H-PB; electrochemical performance of hard carbon anode and Na-ion full batteries; a performance summary of similar Prussian blue electrodes reported recently for SIBs (PDF)

■ AUTHOR INFORMATION

Corresponding Authors

Qi Li – State Key Laboratory of Advanced Technology for Materials Synthesis and Processing, Wuhan University of Technology, Wuhan 430070, Hubei, P.R. China; Foshan Xianhu Laboratory of the Advanced Energy Science and Technology Guangdong Laboratory, Xianhu Hydrogen Valley, Foshan 528200, Guangdong, China; orcid.org/0000-0001-6271-8147; Email: qi.li@whut.edu.cn

Ya You – State Key Laboratory of Advanced Technology for Materials Synthesis and Processing, Wuhan University of Technology, Wuhan 430070, Hubei, P.R. China; orcid.org/0000-0002-2069-5212; Email: youya@whut.edu.cn

Liqliang Mai – State Key Laboratory of Advanced Technology for Materials Synthesis and Processing, Wuhan University of Technology, Wuhan 430070, Hubei, P.R. China; Foshan Xianhu Laboratory of the Advanced Energy Science and Technology Guangdong Laboratory, Xianhu Hydrogen Valley, Foshan 528200, Guangdong, China; orcid.org/0000-0003-4259-7725; Email: mlq518@whut.edu.cn

Authors

Mingsheng Qin – State Key Laboratory of Advanced Technology for Materials Synthesis and Processing, Wuhan University of Technology, Wuhan 430070, Hubei, P.R. China; orcid.org/0000-0002-8039-2440

Wenhao Ren – School of Chemistry, Faculty of Science, The University of New South Wales, Sydney, New South Wales 2052, Australia

Ruixuan Jiang – State Key Laboratory of Advanced Technology for Materials Synthesis and Processing, Wuhan University of Technology, Wuhan 430070, Hubei, P.R. China

Xuhui Yao – State Key Laboratory of Advanced Technology for Materials Synthesis and Processing, Wuhan University of Technology, Wuhan 430070, Hubei, P.R. China

Shiqi Wang – State Key Laboratory of Advanced Technology for Materials Synthesis and Processing, Wuhan University of Technology, Wuhan 430070, Hubei, P.R. China

Complete contact information is available at: <https://pubs.acs.org/doi/10.1021/acsami.0c20067>

Author Contributions

The manuscript was written through contributions of all authors. All authors have given approval to the final version of the manuscript.

Notes

The authors declare no competing financial interest.

■ ACKNOWLEDGMENTS

This work was supported by the National Natural Science Foundation of China (21805219, 51832004, 51521001 and 51902238), the National Key Research and Development Program of China (2016YFA0202603), the program of Introducing Talents of Discipline to Universities (B17034), Foshan Xianhu Laboratory of the Advanced Energy Science and Technology Guangdong Laboratory (XHT2020-003), The Fundamental Research Funds for the Central Universities (205201018, 2020-CLSF-A1-01), and National innovation and entrepreneurship training program for college students (S202010497266).

■ REFERENCES

- (1) Chu, S.; Cui, Y.; Liu, N. The Path Towards Sustainable Energy. *Nat. Mater.* **2017**, *16*, 16–22.
- (2) Xiong, Q.; Huang, G.; Zhang, X. High-Capacity and Stable Li-O₂ Batteries Enabled by a Trifunctional Soluble Redox Mediator. *Angew. Chem., Int. Ed.* **2020**, *59*, 19311–19319.
- (3) Meng, J.; He, Q.; Xu, L.; Zhang, X.; Liu, F.; Wang, X.; Li, Q.; Xu, X.; Zhang, G.; Niu, C.; Xiao, Z.; Liu, Z.; Zhu, Z.; Zhao, Y.; Mai, L. Identification of Phase Control of Carbon-Confined Nb₂O₅ Nanoparticles toward High-Performance Lithium Storage. *Adv. Energy Mater.* **2019**, *9*, 1802695.
- (4) Cong, Y.; Tang, Q.; Wang, X.; Liu, M.; Liu, J.; Geng, Z.; Cao, R.; Zhang, X.; Zhang, W.; Huang, K.; Feng, S. Silver-Intermediated Perovskite La_{0.9}FeO_{3-δ} toward High-Performance Cathode Catalysts for Nonaqueous Lithium-Oxygen Batteries. *ACS Catal.* **2019**, *9*, 11743–11752.
- (5) Vaalma, C.; Buchholz, D.; Weil, M.; Passerini, S. A Cost and Resource Analysis of Sodium-Ion Batteries. *Nat. Rev. Mater.* **2018**, *3*, 18013.
- (6) Ren, W.; Zhu, Z.; An, Q.; Mai, L. Emerging Prototype Sodium-Ion Full Cells with Nanostructured Electrode Materials. *Small* **2017**, *13*, 1604181.
- (7) Wang, S.; Zhu, Y.; Yan, J.; Zhang, X. P3-Type K_{0.32}Fe_{0.35}Mn_{0.65}O₂·0.39H₂O: a Promising Cathode for Na-Ion Full Batteries. *J. Mater. Chem. A* **2018**, *6*, 13075–13081.
- (8) Xu, Y.; Wei, Q.; Xu, C.; Li, Q.; An, Q.; Zhang, P.; Sheng, J.; Zhou, L.; Mai, L. Layer-by-Layer Na₃V₂(PO₄)₃ Embedded in Reduced Graphene Oxide as Superior Rate and Ultralong-Life Sodium-Ion Battery Cathode. *Adv. Energy Mater.* **2016**, *6*, 1600389.
- (9) Shen, L.; Jiang, Y.; Liu, Y.; Ma, J.; Sun, T.; Zhu, N. High-Stability Monoclinic Nickel Hexacyanoferrate Cathode Materials for Ultrafast Aqueous Sodium Ion Battery. *Chem. Eng. J.* **2020**, *388*, 124228.
- (10) Sun, Y.; Guo, S.; Zhou, H. Exploration of Advanced Electrode Materials for Rechargeable Sodium-Ion Batteries. *Adv. Energy Mater.* **2019**, *9*, 1800212.
- (11) Hurlbutt, K.; Wheeler, S.; Capone, I.; Pasta, M. Prussian Blue Analogs as Battery Materials. *Joule* **2018**, *2*, 1950–1960.
- (12) Goda, E. S.; Lee, S.; Sohail, M.; Yoon, K. R. Prussian Blue and Its Analogues as Advanced Supercapacitor Electrodes. *J. Energy Chem.* **2020**, *50*, 206–229.
- (13) Su, D.; Mcdonagh, A. M.; Qiao, S.; Wang, G. High-Capacity Aqueous Potassium-Ion Batteries for Large-Scale Energy Storage. *Adv. Mater.* **2017**, *29*, 1604007.
- (14) Xu, Y.; Ou, M.; Liu, Y.; Xu, J.; Sun, X.; Fang, C.; Li, Q.; Han, J.; Huang, Y. Crystallization-Induced Ultrafast Na-Ion Diffusion in Nickel Hexacyanoferrate for High-Performance Sodium-Ion Batteries. *Nano Energy* **2020**, *67*, 104250.

- (15) Wu, X.; Luo, Y.; Sun, M.; Qian, J.; Cao, Y.; Ai, X.; Yang, H. Low-Defect Prussian Blue Nanocubes as High Capacity and Long Life Cathodes for Aqueous Na-Ion Batteries. *Nano Energy* **2015**, *13*, 117–123.
- (16) Ren, W.; Qin, M.; Zhu, Z.; Yan, M.; Li, Q.; Zhang, L.; Liu, D.; Mai, L. Activation of Sodium Storage Sites in Prussian Blue Analogues via Surface Etching. *Nano Lett.* **2017**, *17*, 4713–4718.
- (17) Chen, R.; Huang, Y.; Xie, M.; Zhang, Q.; Zhang, X.; Li, L.; Wu, F. Preparation of Prussian Blue Submicron Particles with a Pore Structure by Two-Step Optimization for Na-Ion Battery Cathodes. *ACS Appl. Mater. Interfaces* **2016**, *8*, 16078–16086.
- (18) Huang, Y.; Xie, M.; Zhang, J.; Wang, Z.; Jiang, Y.; Xiao, G.; Li, S.; Li, L.; Wu, F.; Chen, R. A Novel Border-Rich Prussian Blue Synthesized by Inhibitor Control as Cathode for Sodium Ion Batteries. *Nano Energy* **2017**, *39*, 273–283.
- (19) You, Y.; Wu, X.; Yin, Y.; Guo, Y. High-Quality Prussian Blue Crystals as Superior Cathode Materials for Room-Temperature Sodium-Ion Batteries. *Energy Environ. Sci.* **2014**, *7*, 1643–1647.
- (20) Song, J.; Wang, L.; Lu, Y.; Liu, J.; Guo, B.; Xiao, P.; Lee, J. J.; Yang, X.; Henkelman, G.; Goodenough, J. B. Removal of Interstitial H₂O in Hexacyanometalates for a Superior Cathode of a Sodium-Ion Battery. *J. Am. Chem. Soc.* **2015**, *137*, 2658–2664.
- (21) Sun, H.; Sun, H.; Wang, W.; Jiao, H.; Jiao, S. Fe₄[Fe(CN)₆]₃: a Cathode Material for Sodium-Ion Batteries. *RSC Adv.* **2014**, *4*, 42991–42995.
- (22) Qin, M.; Ren, W.; Meng, J.; Wang, X.; Yao, X.; Ke, Y.; Li, Q.; Mai, L. Realizing Superior Prussian Blue Positive Electrode for Potassium Storage via Ultrathin Nanosheet Assembly. *ACS Sustainable Chem. Eng.* **2019**, *7*, 11564–11570.
- (23) Chen, R.; Huang, Y.; Xie, M.; Wang, Z.; Ye, Y.; Li, L.; Wu, F. Chemical Inhibition Method to Synthesize Highly Crystalline Prussian Blue Analogs for Sodium-Ion Battery Cathodes. *ACS Appl. Mater. Interfaces* **2016**, *8*, 31669–31676.
- (24) Wang, W.; Gang, Y.; Hu, Z.; Yan, Z.; Li, W.; Li, Y.; Gu, Q.-F.; Wang, Z.; Chou, S.-L.; Liu, H.-K.; Dou, S.-X. Reversible Structural Evolution of Sodium-Rich Rhombohedral Prussian Blue for Sodium-Ion Batteries. *Nat. Commun.* **2020**, *11*, 980.
- (25) Ren, W.; Zhu, Z.; Qin, M.; Chen, S.; Yao, X.; Li, Q.; Xu, X.; Wei, Q.; Mai, L.; Zhao, C. Prussian White Hierarchical Nanotubes with Surface-Controlled Charge Storage for Sodium-Ion Batteries. *Adv. Funct. Mater.* **2019**, *29*, 1806405.
- (26) Buser, H. J.; Schwarzenbach, D.; Petter, W.; Ludi, A. The Crystal Structure of Prussian Blue: Fe₄[Fe(CN)₆]₃·xH₂O. *Inorg. Chem.* **1977**, *16*, 2704–2710.
- (27) You, Y.; Yu, X. Q.; Yin, Y.; Nam, K.; Guo, Y. Sodium Iron Hexacyanoferrate with High Na Content as a Na-Rich Cathode Material for Na-Ion Batteries. *Nano Res.* **2015**, *8*, 117–128.
- (28) Qian, J.; Wu, C.; Cao, Y.; Ma, Z.; Huang, Y.; Ai, X.; Yang, H. Prussian Blue Cathode Materials for Sodium-Ion Batteries and Other Ion Batteries. *Adv. Energy Mater.* **2018**, *8*, 1702619.
- (29) Phadke, S.; Mysyk, R.; Anouti, M. Effect of Cation (Li⁺, Na⁺, K⁺, Rb⁺, Cs⁺) in Aqueous Electrolyte on the Electrochemical Redox of Prussian Blue Analogue (PBA) Cathodes. *J. Energy Chem.* **2020**, *40*, 31–38.
- (30) Huang, B.; Liu, Y.; Lu, Z.; Shen, M.; Zhou, J.; Ren, J.; Li, X.; Liao, S. Prussian Blue K₂FeFe(CN)₆ Doped with Nickel as a Superior Cathode: an Efficient Strategy to Enhance Potassium Storage Performance. *ACS Sustainable Chem. Eng.* **2019**, *7*, 16659–16667.
- (31) Wang, M.; Wang, H.; Zhang, H.; Li, X. Aqueous K-Ion Battery Incorporating Environment-Friendly Organic Compound and Berlin Green. *J. Energy Chem.* **2020**, *48*, 14–20.
- (32) Fu, H.; Liu, C.; Zhang, C.; Ma, W.; Wang, K.; Li, Z.; Lu, X.; Cao, G. Enhanced Storage of Sodium Ions in Prussian Blue Cathode Material Through Nickel Doping. *J. Mater. Chem. A* **2017**, *5*, 9604–9610.
- (33) Barsan, M. M.; Butler, I. S.; Fitzpatrick, J.; Gilson, D. F. R. High-Pressure Studies of the Micro-Raman Spectra of Iron Cyanide Complexes: Prussian Blue (Fe₄[Fe(CN)₆]₃), Potassium Ferricyanide (K₃[Fe(CN)₆]), and Sodium Nitroprusside (Na₂[Fe(CN)₅(NO)]·2H₂O). *J. Raman Spectrosc.* **2011**, *42*, 1820–1824.
- (34) Morant-Giner, M.; Sanchis-Gual, R.; Romero, J.; Alberola, A.; Garcia-Cruz, L.; Agouram, S.; Galbiati, M.; Padial, N. M.; Waerenborgh, J. C.; Marti-Gastaldo, C.; Tatay, S.; Forment-Aliaga, A.; Coronado, E. Prussian Blue@MoS₂ Layer Composites as Highly Efficient Cathodes for Sodium- and Potassium-Ion Batteries. *Adv. Funct. Mater.* **2018**, *28*, 1706125.
- (35) Xie, B.; Zuo, P.; Wang, L.; Wang, J.; Huo, H.; He, M.; Shu, J.; Li, H.; Lou, S.; Yin, G. Achieving Long-Life Prussian Blue Analogue Cathode for Na-Ion Batteries via Triple-Cation Lattice Substitution and Coordinated Water Capture. *Nano Energy* **2019**, *61*, 201–210.
- (36) Samain, L.; Gilbert, B.; Grandjean, F.; Long, G. J.; Strivay, D. Redox Reactions in Prussian Blue Containing Paint Layers as a Result of Light Exposure. *J. Anal. At. Spectrom.* **2013**, *28*, 524–535.
- (37) Yang, D.; Xu, J.; Liao, X.-Z.; Wang, H.; He, Y.-S.; Ma, Z.-F. Prussian Blue Without Coordinated Water as a Superior Cathode for Sodium-Ion Batteries. *Chem. Commun.* **2015**, *51*, 8181–8184.
- (38) Tang, X.; Liu, H.; Su, D.; Notten, P. H. L.; Wang, G. Hierarchical Sodium-Rich Prussian Blue Hollow Nanospheres as High-Performance Cathode for Sodium-Ion Batteries. *Nano Res.* **2018**, *11*, 3979–3990.
- (39) Wu, X.; Wu, C.; Wei, C.; Hu, L.; Qian, J.; Cao, Y.; Ai, X.; Wang, J.; Yang, H. Highly Crystallized Na₂CoFe(CN)₆ with Suppressed Lattice Defects as Superior Cathode Material for Sodium-Ion Batteries. *ACS Appl. Mater. Interfaces* **2016**, *8*, 5393–5399.
- (40) Mao, Y.; Chen, Y.; Qin, J.; Shi, C.; Liu, E.; Zhao, N. Capacitance Controlled, Hierarchical Porous 3D Ultra-Thin Carbon Networks Reinforced Prussian Blue for High Performance Na-Ion Battery Cathode. *Nano Energy* **2019**, *58*, 192–201.
- (41) Ren, W.; Chen, X.; Zhao, C. Ultrafast Aqueous Potassium-Ion Batteries Cathode for Stable Intermittent Grid-Scale Energy Storage. *Adv. Energy Mater.* **2018**, *8*, 1801413.
- (42) Li, W.; Han, C.; Xia, Q.; Zhang, K.; Chou, S.; Kang, Y. M.; Wang, J.; Liu, H. K.; Dou, S. X. Remarkable Enhancement in Sodium-Ion Kinetics of NaFe₂(CN)₆ by Chemical Bonding with Graphene. *Small Methods* **2018**, *2*, 1700346.
- (43) You, Y.; Yao, H.; Xin, S.; Yin, Y.; Zuo, T.; Yang, C.; Guo, Y.; Cui, Y.; Wan, L.; Goodenough, J. B. Subzero-Temperature Cathode for a Sodium-Ion Battery. *Adv. Mater.* **2016**, *28*, 7243–7248.
- (44) Zhang, C.; Xu, Y.; Zhou, M.; Liang, L.; Dong, H.; Wu, M.; Yang, Y.; Lei, Y. Potassium Prussian Blue Nanoparticles: a Low-Cost Cathode Material for Potassium-Ion Batteries. *Adv. Funct. Mater.* **2017**, *27*, 1604307.
- (45) Li, W.; Zhang, F.; Xiang, X.; Zhang, X. Electrochemical Properties and Redox Mechanism of Na₂Ni_{0.4}Co_{0.6}Fe(CN)₆ Nanocrystallites as High-Capacity Cathode for Aqueous Sodium-Ion Batteries. *J. Phys. Chem. C* **2017**, *121*, 27805–27812.
- (46) Luo, D.; Lei, P.; Tian, G.; Huang, Y.; Ren, X.; Xiang, X. Insight Into Electrochemical Properties and Reaction Mechanism of a Cobalt-Rich Prussian Blue Analogue Cathode in a NaSO₃CF₃ Electrolyte for Aqueous Sodium-Ion Batteries. *J. Phys. Chem. C* **2020**, *124*, 5958–5965.
- (47) Ren, W.; Yao, X.; Niu, C.; Zheng, Z.; Zhao, K.; An, Q.; Wei, Q.; Yan, M.; Zhang, L.; Mai, L. Cathodic Polarization Suppressed Sodium-Ion Full Cell with a 3.3 V High-Voltage. *Nano Energy* **2016**, *28*, 216–223.